Monthly Notices of the ROYAL ASTRONOMICAL SOCIETY

MNRAS **547,** 1–13 (2026) https://doi.org/10.1093/mnras/stag228
Advance Access publication 2026 February 04

The polytropic behaviour and turbulence properties of sub-Alfvénic intervals

Komal Choraghe [1]★ Wageesh Mishra [1,2] and Soumyaranjan Khuntia [1,2]

[1]*Indian Institute of Astrophysics, II Block, Koramangala, Bengaluru 560034, India*
[2]*Pondicherry University, R.V. Nagar, Kalapet 605014, Puducherry, India*

Accepted 2026 January 29. Received 2026 January 28; in original form 2025 August 2

ABSTRACT

The solar wind at 1 au is primarily super-Alfvénic, but rare instances occur when the Alfvén speed surpasses the solar wind speed, resulting in occurrences of sub-Alfvénic intervals. During sub-Alfvénic intervals, the solar wind no longer creates a bow shock around Earth, allowing for a direct interaction between the solar wind and Earth's magnetopause. The thermal properties and turbulence characteristics of such rarely observed sub-Alfvénic regions at 1 au are not well understood. Our study comprehensively investigates sub-Alfvénic intervals observed from 1995 to 2023 and identifies a total of eleven such distinct regions embedded within solar wind streams and interplanetary coronal mass ejections (ICMEs). We focus on examining the thermodynamic properties of these regions by using the polytropic index and compare them with nearby super-Alfvénic regions. We find a transition in polytropic behaviour from super-Alfvénic to sub-Alfvénic intervals. Interestingly, we observed a bimodal distribution in the polytropic index, characterized by two distinct states: (i) sub- to super-adiabatic ($\alpha > 1$) and (ii) non-adiabatic ($\alpha < 1$). The presence of a non-adiabatic state at 1 au strongly suggests that heating dynamics is a significant factor influencing the thermodynamic state of the solar wind at this distance. We also investigated turbulence properties, and it indicates that turbulence is lower in sub-Alfvénic flow compared to neighboring super-Alfvénic regions, suggesting different processes are involved in these regions.

Key words: Sun: coronal mass ejections (CMEs) – solar wind.

1 INTRODUCTION

The solar wind at a distance of 1 au from the Sun predominantly exhibits a highly super-Alfvénic nature, characterized by an average Alfvén Mach number (M_A) typically greater than 10 (J. E. Borovsky, M. H. Denton & C. W. Smith 2019; R. Bandyopadhyay et al. 2022). However, there are rare instances where the Alfvén speed surpasses the solar wind speed, leading to conditions termed as sub-Alfvénic regions. These sub-Alfvénic intervals are characterized by a significantly reduced Alfvén Mach number, primarily due to the exceptionally low-solar wind density (G.-L. Zhang 1996; C. W. Smith et al. 2001; A. V. Usmanov et al. 2005). When the Earth's magnetosphere encounters a low-density sub-Alfvénic solar wind, its configuration undergoes significant transformations (E. Chané et al. 2021). Under such conditions, the usual bow shock around Earth disappears, allowing the solar wind to directly interact with Earth's magnetopause. There are several reports of observing sub-Alfvénic intervals in the solar wind and interplanetary coronal mass ejection (ICME). For example, in 1979, three very low-density events were recorded at 1 au, potentially signifying one of the initial identifications of sub-Alfvénic intervals (J. T. Gosling et al. 1982; N. U. Crooker et al. 2000; E. Chané et al. 2021). Following this, A. V. Usmanov et al. (2005) identified cases of sub-Alfvénic solar wind intervals that occurred between 1963 to 2003. More recently, R. Hajra & B. T. Tsurutani (2022) conducted a comprehensive study, compiling a list of these transients from 1973 to 2020 using data from multiple spacecraft. Numerous studies have identified notable implications and correlations associated with sub-Alfvénic solar wind intervals, such as C. W. Smith et al. (2001) reported a suppression of magnetic field fluctuations in sub-Alfvénic solar winds, while P. Janardhan et al. (2008) investigated three low-density events, including the 2002 May event, and suggested that these may be linked to transient coronal holes visible at the solar disc centre. N. Lugaz et al. (2016) documented a rapid and significant depletion of electrons in the outer radiation belt during such an event. Recently, H. Hasegawa et al. (2024) proposed that magnetopause reconnection under sub-Alfvénic solar wind was more efficient than under normal super-Alfvénic solar wind conditions. Previous studies have proposed several mechanisms to explain the generation of sub-Alfvénic intervals. G.-L. Zhang (1996) suggested three possible circumstances that contribute to the generation of sub-Alfvénic flow: (1) an extremely fast solar wind stream overtaking the field inversion boundary within the interaction region of a strong magnetic field, (2) a quasi-magnetic cloud with a rotating field embedded in a quiet solar wind, or (3) a quasi-static low-speed solar wind with a magnetic field in

★ E-mail: komal.c11@gmail.com

the ecliptic plane. E. Chané et al. (2021) also reported that the overexpansion of an ICME during its propagation from the Sun to Earth could contribute to such low-density events.

Certain solar wind conditions can alter geometry of the bow shock's geometry, or even make it disappear altogether. Previous studies support this view; for example, A. P. Dimmock et al. (2017) demonstrated, using THEMIS (Time History of Events and Macroscale Interactions during Substorms) and (Magnetospheric Multiscale) MMS observations that variation in ion temperature within Earth's magnetosheath depends on the bow shock geometry. J.-S. Park et al. (2019) further extended this investigation using THEMIS measurements and reported dependence of the relationship between ion temperature and ion density variations (change in thermodynamic state) in the magnetosheath on the bow shock geometry. Since sub-Alfvénic solar wind conditions have the potential to weaken or may cause the bow shock to disappear, it is therefore essential to examine the associated changes in thermodynamic states, as variations in these states lead to distinct plasma behaviours. The thermodynamic properties of sub-Alfvénic intervals can be analysed by estimating their polytropic state. In many cases, plasma density and temperature are found to correlate with different values of the polytropic index (α), indicating varying thermodynamic states (T. L. Totten, J. W. Freeman & S. Arya 1995; G. Nicolaou, G. Livadiotis & X. Moussas 2014; G. Livadiotis & M. I. Desai 2016; G. Livadiotis 2016; S. Khuntia et al. 2023, 2024). This provides a macroscopic framework to relate plasma moments, allowing for examining plasma transitions from one state to another. The polytropic equation for an ideal gas is expressed as.

$$P \cdot N^{-\alpha} = T \cdot N^{(1-\alpha)} = constant \quad (1)$$

Polytropic analysis involves the proton temperature (T), density (N), and thermal pressure (P) of the plasma. The polytropic expression for the logarithms of these thermal variables becomes linear, enabling a straightforward estimation of the polytropic index (α) by examining the data sets of log (T) versus log (N). For protons, the degree of freedom is considered as three. Equation (1) is only valid under the assumption of a sufficiently homogeneous fluid subregion. In realistic solar-wind observations, it is not feasible to continuously follow a single fluid element, as a spacecraft can not track an individual plasma parcel over time. To overcome this limitation, we employ the Bernoulli integral [see Section 2.2(iii)] as a practical alternative to the otherwise an unattainable task of tracing a specific fluid element. This approach enables us to assume that, a nearly constant Bernoulli expression over some interval indicates that the spacecraft is traversing plasma parcels originating from the same or closely related flow lines within a sufficiently homogeneous solar-wind subdomain. Near 1 au, the polytropic index of the solar wind is approximately equivalent to the value associated with an adiabatic process ($\alpha = 5/3$) (T. L. Totten et al. 1995; G. Livadiotis 2019). Numerous investigations have explored the polytropic index of the solar wind. For instance, B. Durney (1972) presented a theoretical study of stellar wind and examined in the case of polytropic relation between pressure and density in the presence of a magnetic field. In contrast, (G. Nicolaou et al. 2014) performed a statistical assessment of polytropic behaviour in the solar wind at 1 au. More recently, T. Ervin et al. (2024) using PSP observations, demonstrated that the expansion of near-subsonic solar wind plasma is not governed solely by a thermally driven polytropic process, but the magnetic field is also considered. Furthermore, Y. Jiao et al. (2024) derived the polytropic index using both modeling and PSP observations, showing that the polytropic index varies across solar wind intervals originating from different source regions, including coronal hole (CH) interiors, streamers, and low-Mach-number boundary layers (LMBLs). In addition to the ambient solar wind, the polytropic properties of ICMEs have also been investigated. For example, (W. Mishra et al. 2020) analysed the polytropic index of ICMEs, while M. A. Dayeh & G. Livadiotis (2022) conducted a statistical examination of the polytropic behaviour of ICME substructures. Moreover, S. Khuntia, W. Mishra & A. Agarwal (2025) examined the polytropic behaviour of both protons and electrons during an extreme geomagnetic storm driven by ICME-ICME interaction. Despite these extensive efforts, the thermodynamic state of sub-Alfvénic regions embedded within solar wind streams and ICMEs at 1 au remain largely unexplored.

The solar wind is generally expected to expand into the heliosphere with minimal energy variation, resulting in cooling due to adiabatic expansion. However, the presence of turbulence can significantly alter this ideal scenario; turbulent heating of the solar wind results in a polytropic index lower than the adiabatic value (G. Livadiotis & D. J. McComas 2023). Through the cascade process, turbulence facilitates energy transfer from large to small scales until it ultimately dissipates (W. H. Matthaeus et al. 1999; L. Sorriso-Valvo et al. 2007; Y. Yang et al. 2019; Z. I. Shaikh et al. 2023b; Z. I. Shaikh 2024). It plays a key role in the governing plasma processes, including plasma heating (B. D. G. Chandran et al. 2013; E. Yordanova et al. 2021), particle acceleration (G. Brunetti & A. Lazarian 2007), and anisotropy (F. Sahraoui et al. 2006; C. H. K. Chen et al. 2010). Therefore, it is important to study the turbulence properties of sub-alfvénic flow. Since turbulence is prevalent in astrophysical plasmas, it has been observed in multiple regions, such as the solar wind (R. Bruno & V. Carbone 2013, 2016), planetary magnetospheres (M. Echim et al. 2021), the interstellar medium (B. G. Elmegreen & J. Scalo 2004), and galaxy clusters (G. Brunetti & A. Lazarian 2007). Generally, the turbulent spectrum is categorized into three scales: the injection scale, the inertial scale, and the dissipation scale. Different spectral characteristics are associated with these scales, including $k_{\rm B}^{-1}$ for the injection scale, $k_B^{-5/3}$ to $k_{\rm B}^{-3/2}$ for the inertial scale, and k_B^{-2} to k_B^{-4} for the dissipation scale (A. Kolmogorov 1941a; R. H. Kraichnan 1965; W. H. Matthaeus et al. 1999; S. D. Bale et al. 2005; W. H. Matthaeus et al. 2007; R. Bruno & V. Carbone 2013; Z. I. Shaikh et al. 2023b). In previous studies extensive research has been conducted on solar wind turbulence at various scales (A. Verdini & M. Velli 2007; A. Verdini, M. Velli & E. Buchlin 2009; R. Bruno & V. Carbone 2013, 2016; D. Telloni et al. 2021; S. Q. Zhao et al. 2022). Earlier investigations of solar wind turbulence at 1 au have been conducted by several researchers. For example, W. H. Matthaeus et al. (1999) carried out a comparative analysis of solar wind turbulence using a theoretical model and Voyager 2 spacecraft observations spanning from 1 au to larger heliocentric distances. While, A. Verdini & M. Velli (2007) studied Alfvénic turbulence, particularly in the solar atmosphere and solar wind by the model at different frequencies. Furthermore, A. Verdini et al. (2009) examined a turbulent spectrum of Alfvén waves by a model from the coronal base to up to 17 solar radii and suggested that reflection and reflection-driven turbulence play a key role in the acceleration of the fast solar wind. Additionally, G. P. Zank et al. (2012) investigated transport of low frequency turbulence by using scale-separated decomposition of the incompressible MHD equations. In particular, S. Q. Zhao et al. (2022) analysed 3D magnetic power spectra in wavevector space to study the anisotropy of

sub-Alfvénic solar wind turbulence at MHD scale using MMS observations at 1 au. While, L. Richard et al. (2024) examined turbulence in magnetic reconnection jets in Earth's magnetotail using MMS data, and demonstrated that signatures of a limited inertial range are present in many reconnection jets. Furthermore, Z. I. Shaikh (2024) reported a statistical study of turbulence properties of ICME flux rope at 1 au. More recently, Parker Solar Probe (PSP) measurements have enabled detailed characterization of turbulence in the near-Sun solar wind. Multiple studies have been carried out during the PSP's close encounters of the solar corona, such as J. C. Kasper et al. (2021) reported one of the first PSP observation of turbulence in sub-Alfvénic solar wind and suggested the source of generation of sub-Alfvénic interval. Furthermore, D. Telloni et al. (2021) investigated the evolution of solar wind turbulence from 0.1 to 1 au utilizing PSP and Solar Orbiter measurements, and have shown that, near Sun plasma evolved as less developed turbulence to fully developed turbulence at 1 au. In addition, G. P. Zank et al. (2022) observed the power spectral index of magnetic field fluctuations in sub-Alfvénic region is $k_B^{-1.52}$ and in super-Alfvénic region is $k_B^{-1.48}$ (at inertial scale) using PSP. However, R. Bandyopadhyay et al. (2022) noticed that, the turbulence in magnetic field fluctuations is high in super-Alfvénic flow as compared to sub-Alfvénic flow using PSP. While, L.-L. Zhao et al. (2022a) presented an analysis of the turbulence cascade rate and correlation function in the sub-Alfvénic solar wind observed by PSP. Additionally, L.-L. Zhao et al. (2022b) observed that power spectrum of the outward-propagating Elsässer z^+ mode steepens at high frequencies while that of the inward-propagating z^- mode flattens in sub-Alfvénic solar wind by PSP. Whereas, J. Zhang et al. (2022) observed power spectra of three (RTN) magnetic field components are close to $k_B^{-3/2}$ at the inertial scale for both sub-Alfvénic and super-Alfvénic regions using PSP. While, G. P. Zank et al. (2024) studied low frequency MHD turbulence (power spectra of density fluctuations) in the sub-Alfvénic flow using PSP. Moreover, T. Ervin et al. (2024) showed turbulence in sub-Alfvénic period is close to $k_B^{-3/2}$ and sub-Alfvénic interval is dominated by outward-propagating Alfvén waves during PSP. Whereas, V. K. Jagarlamudi et al. (2025) noticed that power in the magnetic field fluctuations and the normalized magnetic field fluctuations are considerably lower in the sub-Alfvénic intervals compared with the super-Alfvénic ones, by PSP. In addition, X. Zhu et al. (2025) studied radial evolution of MHD turbulence anisotropy in low mach number solar wind using PSP and Wind spacecrafts. In addition, R. D'Amicis et al. (2025) investigated Alfvénic turbulence in solar wind streams during Solar Orbiter perihelion. Although solar wind turbulence has been extensively investigated, turbulence in sub-Alfvénic flows at 1 au remains poorly understood, with only a limited number of studies available, such as S. Q. Zhao et al. (2022).

Several previous investigations have addressed sub-Alfvénic intervals, focusing on their identification and associated physical properties. For example, A. V. Usmanov et al. (2005) presented a comparative analysis of simulated and observed plasma properties during sub-Alfvénic intervals near 1 au. Furthermore, R. Hajra & B. T. Tsurutani (2022) performed multi-spacecrafts statistically investigation of sub-Alfvénic intervals and structures (like solar wind and ICME) in which it is embedded. While, S. Q. Zhao et al. (2022) studied anisotropy and scaling of sub-Alfvénic solar wind turbulence near Earth using MMS at 1 au. Recent observations of sub-Alfvénic region from PSP, such as G. P. Zank et al. (2022) characterized key physical properties like magnetic helicity, cross-helicity, residual energy and turbulence spectra of sub-Alfvénic solar wind. Furthermore, K. W. Paulson et al. (2023) examined Ion-scale wave-particle interaction within sub-Alfvénic solar wind utilizing PSP. While, L. Ofman et al. (2023) investigated unstable proton and α particle velocity distribution in sub-Alfvénic solar wind using model and PSP observations.

However, these studies leave a gap in our understanding of the thermodynamic and turbulence properties of sub-Alfvénic intervals in detail at 1 au. To address this, the present work aims to (i) investigate the thermodynamic behaviour of sub-Alfvénic intervals in solar wind/ICME, (ii) analyse the transition of the polytropic index from sub-Alfvénic regions to the adjacent super-Alfvénic regions (pre-sub-Alfvénic and post-sub-Alfvénic intervals) and (iii) study the plasma turbulence in sub-Alfvénic and super-Alfvénic regions. This study examines 11 sub-Alfvénic events observed at 1 au, focusing on polytropic behaviour during intervals preceding, within and following the passage of sub-Alfvénic intervals. We also focus on the heating and cooling that occur within these sub-Alfvénic intervals embedded in the solar wind and ICMEs.

2 METHODOLOGY AND OBSERVATIONS

The selected sub-Alfvénic intervals at 1 au analysed in this study are based on two key criteria: the duration of the sub-Alfvénic phase and the availability of high-quality data. We selected only those regions with a time span exceeding 30 minutes, displaying a clear signature of M_A less than one, and for which data were available from the WIND spacecraft. The dataset, covering the period from 1995 to 2023 and encompassing complete solar cycles 23 and 24, was obtained from the Wind Magnetic Fields Investigation (MFI) (R. P. Lepping et al. 1995) and the 3D Plasma Analyser (3DP) (R. P. Lin et al. 1995) instruments, with a 3-s cadence. To conduct this statistical analysis, we preferentially use WIND/3DP data rather than WIND/SWE. This choice is motivated by several factors, including the unavailability of SWE measurements for many of the selected events. In addition, the sub-Alfvénic intervals of interest are typically of very short duration; consequently, after applying the required filtering criteria, the remaining SWE data are often insufficient to yield meaningful results. We took data from the Coordinated Data Analysis Web (CDAWeb). Additionally, WIND MFI data with a 0.092-s cadence are used to study turbulence in both sub-Alfvénic and super-Alfvénic flows. In the following, we describe the identification of sub-Alfénic regions, their polytropic behaviour, and turbulence properties.

2.1 Identification of Sub-Alfvénic intervals

To identify intervals of sub-Alfvénic solar winds, a detailed survey has been conducted on high-resolution solar wind data, measured by the WIND spacecraft. We identified 11 sub-Alfvénic intervals from 1995 to 2023 based on our selection criteria. Some of the events are similar to R. Hajra & B. T. Tsurutani (2022) sub-Alfvénic interval's list. We have only chosen the intervals that represent the signature of the sub-Alfvénic region, i.e. $M_A < 1$ for at least 30 min. However, because of the highly fluctuating nature of the solar wind, the M_A may not consistently remain below 1; therefore, if M_A exceeds or remains equal to 1 and persists for more than one-tenth period of a total sub-Alfvénic time interval, this is considered the end of the sub-Alfvénic interval. To do a comparative study, super-Alfvénic (pre- and

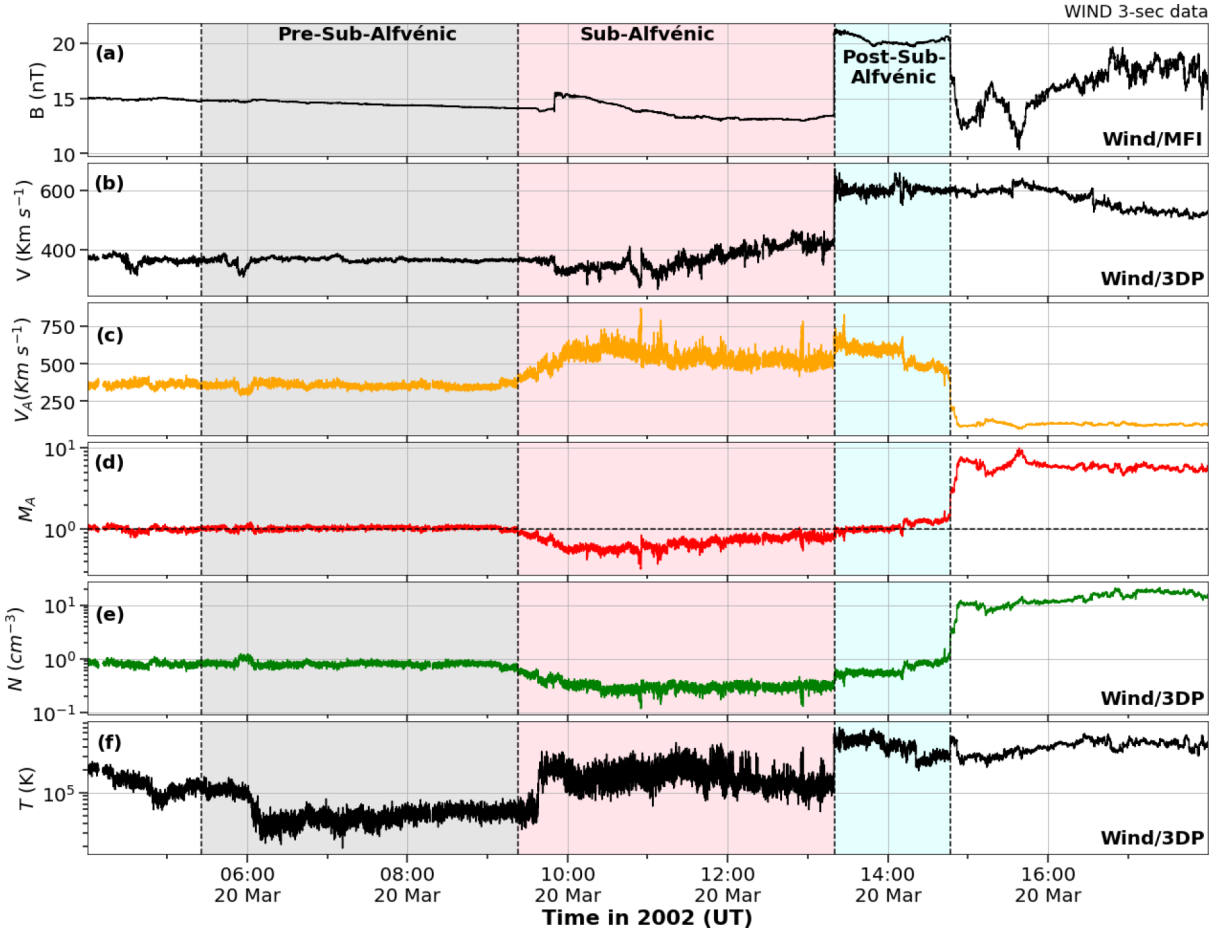

Figure 1. The proton plasma parameters for the event occurred on 2002 March 20, with the three analysed regions denoted as pre-sub-Alfvénic (grey), sub-Alfvénic (pink), and post-sub-Alfvénic (cyan). The top three panels (a), (b), and (c) show averaged magnetic field (B), solar wind speed (V), and Alfvén speed (V_A), respectively. Panels (d), (e), and (f) show Alfvén Mach number (M_A), plasma density (N), and temperature (T), respectively.

post-sub-Alfvénic) regions have the same duration as the sub-Alfvénic region in all events. However, if a sudden transient structure (sudden enhancement in proton density) appears within the super-Alfvénic region *i.e.* pre- and post-sub-Alfvénic regions, then those regions are truncated at the onset of that transient structure.

Fig. 1 represents the solar wind proton plasma parameters of an event that occurred on 2002 March 20. The grey, pink, and cyan shaded regions depict pre-, sub- and post-sub-Alfvénic regions, respectively. This event includes a sub-alfvénic interval of ≈ 4 h characterized by $M_A < 1$ and low proton density (N) and the pre- and post-sub-Alfvénic intervals have duration equal to that of the sub-Alfvénic interval. However, a sudden increase in N, temperature (T), and M_A, along with a sharp decrease in the total magnetic field (B) within the post-sub-Alfvénic interval, marks the onset of another structure, which shortens the interval. In the pre-sub-Alfvénic region, N drops below ≈ 1 cm^{-3}, and Alfvén speed (V_A) becomes comparable to the solar wind bulk speed (V), resulting in $M_A \approx 1$. Within the sub-Alfvénic interval, N drops further to a minimum value ≈ 0.33 cm^{-3}, causing V_A to reach a peak value at ≈ 873 km s^{-1} while the solar wind speed remains low, keeping M_A significantly below 1 for ≈ 4 h. In post-sub-Alfvénic regions N increases and V_A is initially comparable to V and then decreases; thus, the value of M_A initially remains close to 1 and then exceeds unity.

2.2 Estimation of Polytropic Index

The polytropic index is determined for three distinct regions: the pre-sub-Alfvénic interval, the sub-Alfvénic interval, and the post-sub-Alfvénic interval. To estimate the polytropic index, we applied the linear fit model to the logarithms of equation (1) to each interval directly. However, this method provides a poor linear fit with a very low correlation coefficient. Therefore, we used the following steps to determine the polytropic index, as discussed in previous studies (M. Kartalev et al. 2006; C. Katsavrias et al. 2024).

(i) Time interval selection: The polytropic index is calculated over certain time intervals, and, therefore, we chose a moving window of five data points. Windows with fewer than five data points are excluded from the analysis to ensure data integrity. This approach has been validated and designed to minimize the contamination of mixed particle measurements across different streamlines.

(ii) Density–temperature fitting: To estimate the polytropic index (α), we fit the logarithms of temperature ($\log(T)$) and density ($\log(n)$) where the slope equals $\alpha-1$.

(iii) Bernoulli's integral filter: This condition is critical to ensure that the polytropic index is derived from a plasma ensemble that is likely to be coherent along the same streamline. Since

Bernoulli's integral remains constant along a streamline, it can be approximated in the solar wind near 1 au as (G. Livadiotis 2016):

$$\frac{V^2}{2} + \frac{\alpha}{\alpha - 1} \cdot \frac{P}{\rho} + \frac{B^2}{\mu_0 \rho} \quad for\ \alpha \neq 1 \tag{2}$$

$$\frac{V^2}{2} + \ln(\rho) \cdot \frac{P}{\rho} + \frac{B^2}{\mu_0 \rho} \quad for\ \alpha = 1 \tag{3}$$

where V is the proton bulk speed, ρ is the proton mass density, and P is proton thermal pressure. It is important to note that in previous studies, the term alfvén speed is neglected, as this is very small compared to the dynamic speed (G. Nicolaou et al. 2014; G. Nicolaou et al. 2020). However, our research focused on sub-Alfvénic intervals in which Alfvén speed is higher than the dynamic speed, and therefore we have included all three terms i.e. dynamic speed, thermal term, and Alfvén speed term. In this study, we analysed the variability of the Bernoulli integral within each sub-interval of the moving window. Sub-intervals for which the standard deviation exceeded 5 per cent of the mean value were excluded from further analysis.

(iv) Correlation and standard error of the slope filter: A correlation filter was applied to the calculations of the polytropic index. We retain only those values of the polytropic index from sub-intervals for which an absolute value of the Pearson correlation coefficient (density–temperature fitting) is greater than 0.8, and p-values are less than 0.05. Additionally, to exclude the polytropic index corresponding to a high error in the slope of the fitting, we applied three filters to the standard error of the slope. We selected to present our results corresponding to standard error of the slope below 0.3, 0.5, and 1.

(v) For visual clarity, in some sub-intervals where the polytropic index attains values ($\alpha < -10$), these values are excluded only from the histogram visualization. They are, however, fully retained in the dataset used for the computation of the median values.

2.3 Analysis of turbulence

The fluctuation of the magnetic field is a significant parameter for estimating the magnitude of turbulence. Magnetic field fluctuation can be described as

$$\delta B = B - \langle B \rangle \tag{4}$$

Similarly, for individual magnetic field components, the fluctuation is given by $\delta B_i = B_i - \langle B_i \rangle$, where i corresponds to the x, y, and z components (R. Bandyopadhyay et al. 2022; Z. I. Shaikh 2024). The notation $\langle ... \rangle$ represents the average value of the magnetic field for super-Alfvénic and sub-Alfvénic regions separately; here, the super-alfvénic region is combined intervals of pre- and post-sub-Alfvénic period. To analyse the turbulence spectrum, the Fast Fourier Transform (FFT) was applied to the fluctuating magnetic field and its components. The power spectral density (PSD) of the total magnetic field is given by $P_t = |\delta B(f)|^2$, where f represents the frequency. Similarly, the power spectra of the individual components are expressed as $P_x = |\delta B_x(f)|^2$, $P_y = |\delta B_y(f)|^2$, $P_z = |\delta B_z(f)|^2$, here $\delta B_x(f)$, $\delta B_y(f)$, $\delta B_z(f)$ are Fourier-transformed magnetic field components. The power spectral density of the trace of magnetic field fluctuations is denoted by $P_{tr} = P_x + P_y + P_z$.

Figs 2 (a) and (b) represent $P_{\rm tr}$ for the event that occurred on 2002 March 20, corresponding to two regions: super-Alfvénic (encompassing both pre- and post-sub-Alfvénic regions) and sub-Alfvénic, respectively. The logarithm of $P_{\rm tr}$ is fitted over two distinct ranges: the inertial scale (1 mHz to 0.16 Hz) and the dissipation scale (0.2 to 1 Hz) (C. Chen et al. 2020; Z. I. Shaikh 2024). The spectral index ($k_{\rm B}$) in the inertial scale is approximately -1.63 for the super-Alfvénic and -1.56 for the sub-Alfvénic intervals. In the dissipation scale, $k_{\rm B}$ is approximately -2.4 for super-Alfvénic and -2.7 for the sub-Alfvénic intervals. The correlation coefficient for both fittings exceeds 0.8. In the inertial range, the spectral slope of $f^{-1.6}$ in the super-Alfvénic interval suggests that turbulence follows a Kolmogorov-like spectrum ($\simeq f^{-5/3}$) (A. Kolmogorov 1941b). However, the sub-Alfvénic interval exhibits a power law scaling of $f^{-3/2}$, indicating turbulence behaviour closer to the Iroshnikov-Kraichnan (IK) scaling ($f^{-3/2}$) (P. S. Iroshnikov 1964; R. H. Kraichnan 1965). Furthermore, in the super-alfvénic and sub-alfvénic regions, we noticed that the spectral break is close to the proton cyclotron frequency ($f_{ci} = \Omega_i/2\pi = 0.26$ Hz where $\Omega_i = q_i B/m_i$), which is shown by a vertical black line. In super- and sub-alfvénic both the regions spectral breaks are far away from the frequency corresponding to an ion inertial length $\simeq 0.8$ Hz ($f_{di} = V_i/2\pi d_i \simeq 0.8$ Hz and $d_i = c/w_{pi} = \sqrt{N_i q_i/(\epsilon_0 m_i)}$ is an ion plasma frequency) exhibited by a vertical brown line and ion Larmor radius $\simeq 2.0$ Hz ($f_{\rho_i} = V_i/2\pi\rho_i \simeq 2$ Hz and $\rho_i = V_{thi\perp}/\Omega_i$) depicted by a vertical green line (C. H. K. Chen et al. 2014).

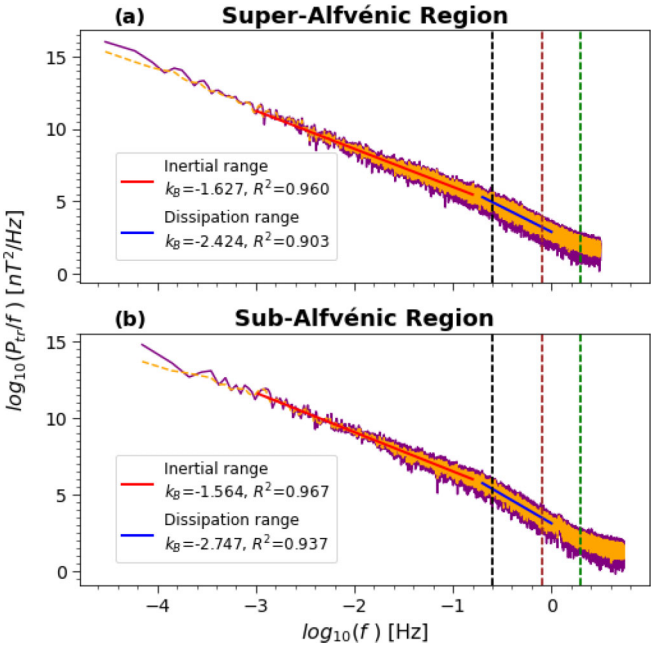

Figure 2. The (a) and (b) display the FFT-based power spectral density of the trace of magnetic field data for the event on 2002 March 20, during super-Alfvénic and sub-Alfvénic intervals, respectively. The solid red and blue lines represent the fitted power laws for the inertial scale (1 mHz to 0.16 Hz) and the dissipation scale (0.2 to 1 Hz), respectively. The vertical dash black, brown, and green lines represent proton cyclotron (f_{ci}), ion inertial length (f_{di}), and ion Larmor radius (f_{ρ_i}), respectively. $k_{\rm B}$ represents the spectral index.

3 RESULTS AND DISCUSSION

3.1 Superposed epoch analysis of sub- and super-Alfvénic regions

Superposed epoch analysis (SEA) functions as a robust statistical technique to identify recurring patterns in physical parameters associated with specific types of events. The process involves

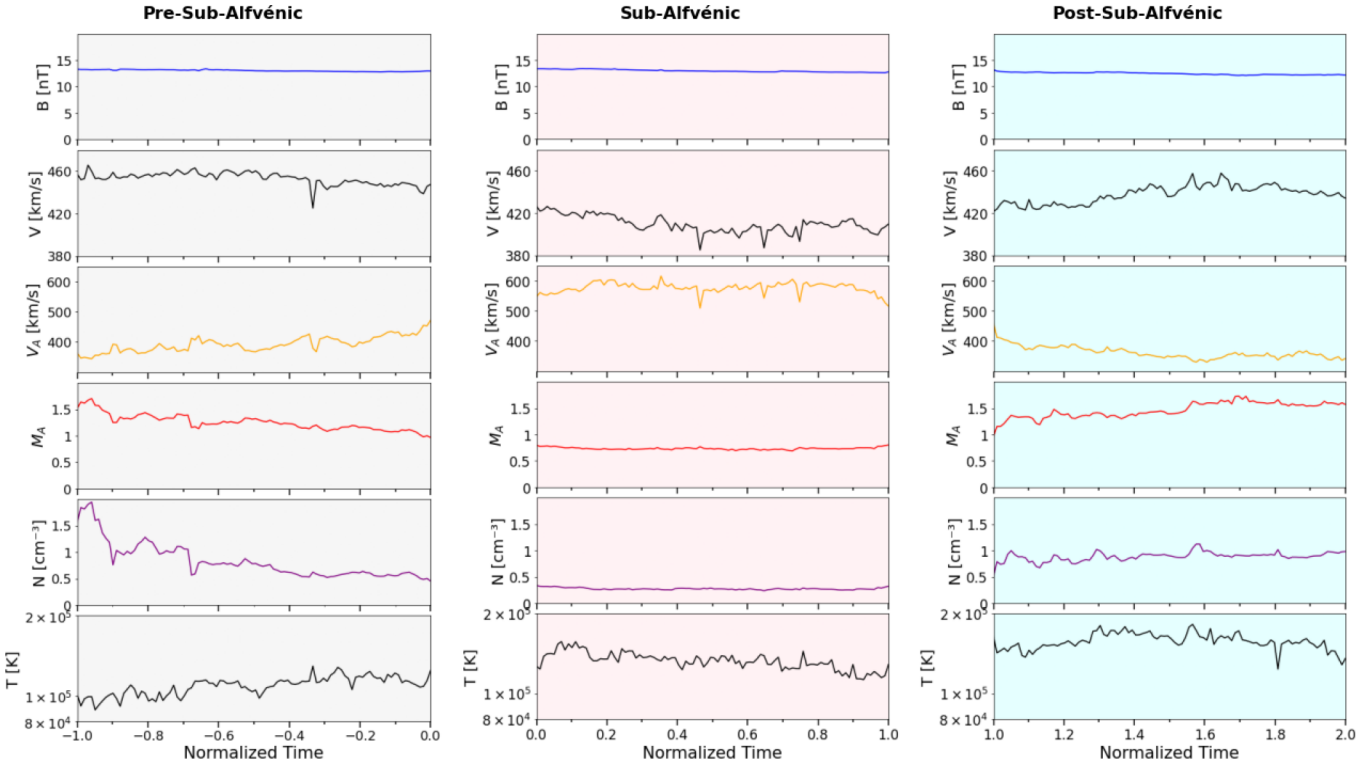

Figure 3. The superposed epoch analysis (SEA) method applied to proton parameters for all identified events. The pre-sub-Alfvénic (grey), sub-Alfvénic (pink), and post-sub-Alfvénic (cyan) regions are plotted against their respective normalized time intervals.

extracting temporal profiles of physical parameters around the epochs of interest, then normalizing the time for each event so that they can be directly compared. Furthermore, superimposing these time-aligned profiles and computing their average enables the extraction of common features across all events while suppressing random fluctuations. SEA has been extensively applied to study different structures, such as solar wind streams (Y. I. Yermolaev et al. 2015) and corotating interaction regions (J. E. Borovsky & M. H. Denton 2010). It also significantly contributes to understanding transient phenomena like ICMEs (F. Regnault et al. 2020) and their substructures (J. J. Masías-Meza et al. 2016), as well as the typical profile of geomagnetic storms (N. Yokoyama & Y. Kamide 1997; Y. I. Yermolaev et al. 2010; J. A. Hutchinson, D. M. Wright & S. E. Milan 2011; V. Manu et al. 2023). In our study, we applied SEA to each region *i.e.* pre-, sub-, and post-sub-Alfvénic regions individually; each region has a different set of time intervals. The normalized duration of each sub-Alfvénic interval, along with the adjacent pre- and post-sub-Alfvénic intervals, is divided into 100 time bins.

Fig. 3 presents the superposed interplanetary plasma parameters for all analysed events. The normalized time axis is segmented into three distinct phases: the pre-sub-Alfvénic (grey) spanning from −1 to 0, the sub-Alfvénic (pink) from 0 to 1, and the post-sub-Alfvénic (cyan) from 1 to 2. It is important to note that while time normalization provides a standardized framework, the actual duration of each phase vary across individual events. The top panel illustrates a slight reduction in the total magnetic field strength across all three intervals. Within the sub-Alfvénic region, the solar wind speed notably decreases compared to the adjacent super-Alfvénic intervals (pre- and post-sub-Alfvénic intervals), whereas the Alfvén speed exhibits a significant enhancement. Consequently, M_A falls below unity within the sub-Alfvénic region, confirming the sub-Alfvénic nature of the plasma, while it remains greater than unity in the neighboring super-Alfvénic regions. In particular, the proton density in the sub-Alfvénic interval drops to extremely low values (below 0.4 cm^{-3}), in contrast to the relatively higher densities observed in the super-Alfvénic regions. However, the proton temperature remains elevated throughout both sub- and super-Alfvénic intervals.

3.2 Thermal states using polytropic index

The distribution of the polytropic index for the event that occurred on 2002 March 20 is illustrated in Fig. 4, classified into three intervals: (a) pre-sub-Alfvénic, (b) sub-Alfvénic, and (c) post-sub-Alfvénic, these regions are delineated in Fig. 1. In each region, the polytropic index values for the standard error of the slope (σ) less than 1, 0.5, and 0.3 are represented by green, orange, and blue, respectively. The median values of the polytropic index for the cases with $\alpha > 1$ and $\sigma < 0.5$ are 2.61, 2.34, and 2.26 for the pre-, sub-, and post-sub-Alfvénic regions, respectively. Similarly, the values of the polytropic index for $\alpha < 1$ and $\sigma < 0.5$ are −0.38, −1.29, and −0.3 for the respective regions. The decreasing trend in the polytropic index (for $\alpha > 1$) from the pre- to post-sub-Alfvénic regions suggests that plasma cooling processes become less efficient as the spacecraft transitions through the regions in the plasma frame. However, a clear transition in the polytropic values (for $\alpha < 1$) are observable from super- to sub-Alfvénic intervals. Moreover, we noticed that the polytropic behaviour of sub-Alfvénic regions varies at smaller scales (smaller sub-intervals) compared to previous large-scale observations (complete intervals). Our analysis demonstrates that the polytropic

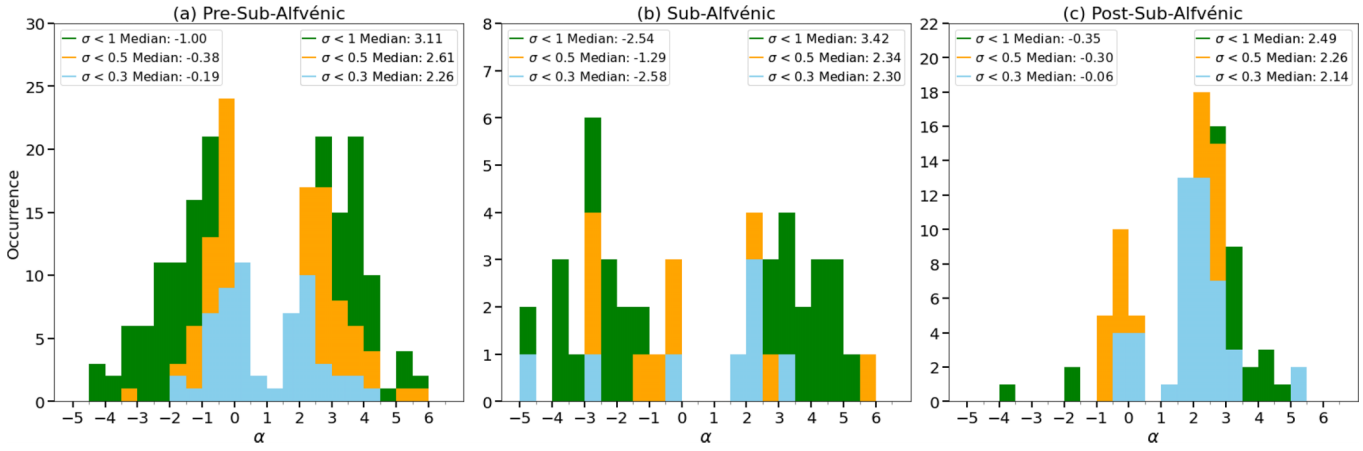

Figure 4. Histograms illustrating the bimodal polytropic distribution for the event on 2002 March 20, across (a) Pre-Sub-Alfvénic, (b) Sub-Alfvénic, and (c) Post-Sub-Alfvénic intervals. Here, α denotes the polytropic index, and σ represents the standard error of the slope. The colors green, orange, and blue indicate standard error of the slope below 1, 0.5, and 0.3, respectively.

index exhibits a predominantly bimodal distribution, with the isothermal state serving as a natural boundary between distinct thermodynamic phases; see Fig. 4. Specifically, the regions where α is below the isothermal state are governed by non-adiabatic processes, indicating a dominance of heating over cooling processes, while α above the isothermal state is presented by sub- to super-adiabatic processes, reflecting a predominance of cooling over heating (V. A. Osherovich et al. 1993; G. Livadiotis 2016; G. Nicolaou, G. Livadiotis & R. T. Wicks 2019; G. Livadiotis & G. Nicolaou 2021; S. Khuntia et al. 2023, 2025). The selection of the isothermal state as the separation boundary is purely based on observations of the values of the polytropic index. This classification provides a robust framework for interpreting the thermodynamic diversity within the solar wind intervals.

Our statistical analysis found a bimodal distribution in almost all cases, as shown in Fig. 5, and the isothermal state acts as the defining boundary in all regions represented by the vertical black line. This figure resembles Fig. 4; however, Fig. 5 incorporates all eleven events to determine the polytropic index and analyse their collective behaviour. Green, orange, and blue indicate standard error of the slope below 1, 0.5, and 0.3, respectively, for pre-, sub, and post-sub-Alfvénic regions. In Fig. 5, two distinct modes are evident in each region, and transitions in the median values of the polytropic index are clearly observed for each standard error of the slope. Table 1 provides two distinct median values of the polytropic index for each region with a standard error of the slope below 0.5. In 10 of 11 events, we observed a change in the median values of the polytropic index (either $\alpha > 1$ or $\alpha < 1$ or both) within the sub-Alfvénic regions, while the polytropic index values in the pre-sub-Alfvénic and post-sub-Alfvénic regions remained unchanged. The remaining event exhibits a transition in the median values of the polytropic index, either an increasing or decreasing trend from pre- to post-sub-Alfvénic regions. Furthermore, a detailed classification of the median value of the polytropic index provides more insights related to the interplanetary structures in which they are embedded, refer to Table 1 (last three columns).

The Sub-Alfvénic intervals occur primarily within ICME-magnetic clouds (MCs) or high-speed streams (HSS), see Table 1 (last column) and Figures in Appendix A and B. We have distinguished events into two types based on their transition in median values of polytropic index from super (Pre & Post)- to sub-Alfvénic intervals (see Table 1): Case 1: super- to sub-Alfvénic transitions in both $\alpha < 1$ and $\alpha > 1$. Case 2: super- to sub-Alfvénic transitions in either $\alpha < 1$ or $\alpha > 1$. In case 1, we observed that, sub-Alfvénic intervals embedded within HSS i.e. events 1, 2, & 7, and also one sub-Alfvénic region embedded within magnetic cloud i.e. event 11 show transition in both super- to sub-Alfvénic transitions in both $\alpha < 1$ and $\alpha > 1$. While in case 2, we observed that sub-Alfvénic regions embedded within ICME-MC i.e. events 3, 4, 5, 8, 9 and 10, these events show a transition in the polytropic index from super to sub-Alfvénic either in $\alpha < 1$ or in $\alpha > 1$. Although, this association is not statistically strong, it hints at a possible linkage between the thermodynamic evolution of sub-Alfvénic intervals and the nature of their embedding interplanetary structures.

At 1 au, several studies have been conducted to analyse the polytropic behaviour of solar wind protons. These studies report an adiabatic plasma with $\alpha \approx 1.6$ (G. Livadiotis & M. I. Desai 2016; G. Livadiotis 2018; G. Nicolaou & G. Livadiotis 2019; G. Nicolaou, G. Livadiotis & M. I. Desai 2021). However, some observations at 1 au have shown super-adiabatic plasma behaviour. For example, G. Nicolaou et al. (2020) reported a super-adiabatic nature of solar wind protons based on high-time-resolution observations by the Parker Solar Probe (PSP). Similarly, Z. I. Shaikh et al. (2023a) observed super-adiabatic alfvénic solar wind, and K. Ghag et al. (2025) identified a super-adiabatic ICME–HSS interaction region. Furthermore, M. A. Dayeh & G. Livadiotis (2022) reported transitions in polytropic states within ICME substructures. Unlike the plasma observations at 1 au, the solar wind protons at larger distances exhibit different behaviour. H. A. Elliott et al. (2019) reported that, $\alpha \approx 1.3$ at ≈ 20 au, and the value of α decreases with radial distance, becoming $\alpha < 1$ beyond 30 au. In support of these observations, G. Livadiotis (2019) suggested that the value of the polytropic index decreases as the heliocentric distance increases. These findings indicate enhanced heating of solar wind protons as they propagate farther from the Sun. Previous observational studies employing similar methodologies have reported a bimodal distribution of the proton polytropic index in solar wind and ICME (super-Alfvénic flow) (G. Nicolaou et al. 2014; C. Katsavrias et al. 2024; S. Khuntia et al. 2025; C. Katsavrias et al. 2025a, b). In these works, the two distributions

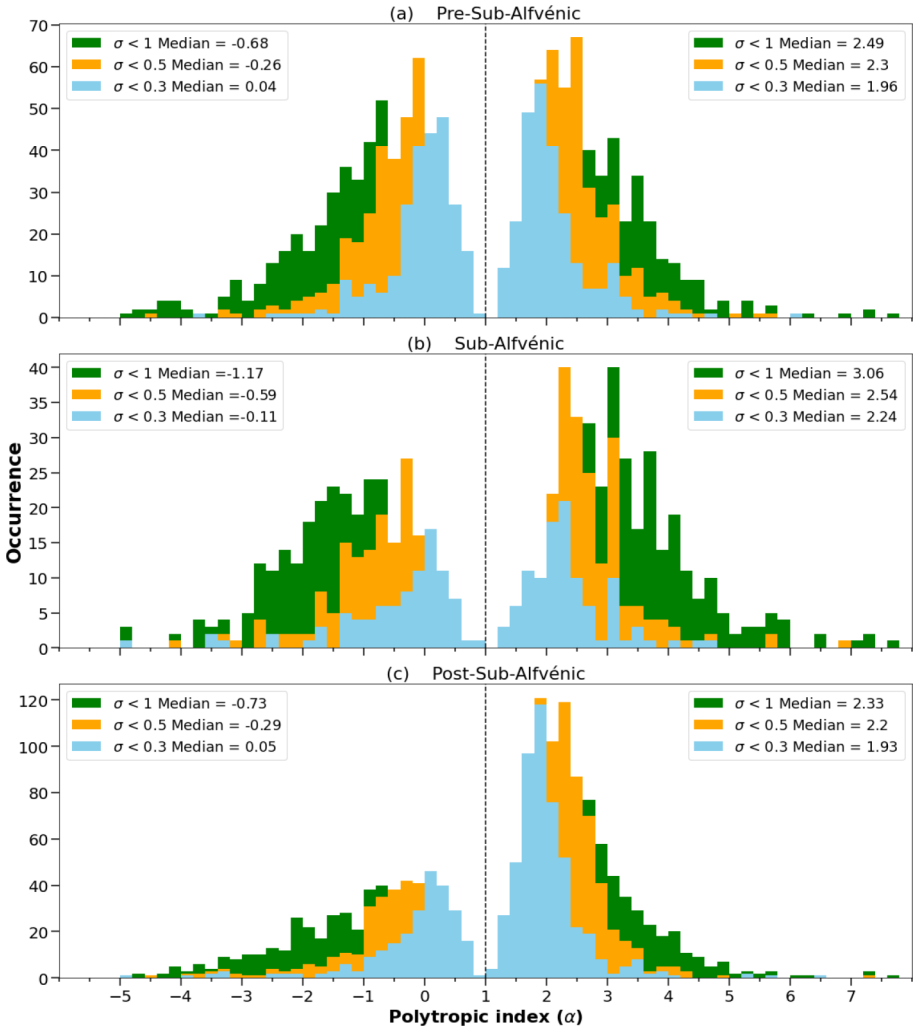

Figure 5. This figure, analogous to Fig. 4, represents the bimodal polytropic distribution for all events. The isothermal state ($\alpha = 1$) acts as a boundary separating the two distinct distribution modes of the polytropic index.

Table 1. This table presents the polytropic index (α) values for standard error of the slope (σ) less than 0.5, corresponding to the selected Pre-sub-Alfvénic, Sub-Alfvénic, and Post-sub-Alfvénic intervals observed during 1995 to 2023.

Sr. No.	Sub-Alfvénic interval Start Time and Stop Time	α <1 (median) [Pre, Sub, Post]	α >1 (median) [Pre, Sub, Post]	IP structure
1	27-04-1999 01:52:28–27-04-1999 06:35:01	[−0.26, −0.98, 0.12]	[2.39, 2.6, 2.25]	HSS
2	11-05-1999 17:34:40–11-05-1999 18:49:22	[−0.54, -, 0.34]	[2.77, 2.3, 2.39]	HSS
3	20-03-2002 09:23:01–20-03-2002 13:20:10	[−0.38, −1.29, −0.3]	[2.61, 2.34, 2.26]	MC
4	24-05-2002 21:01:07–24-05-2002 23:47:19	[−1.31, −1.35, −0.79]	[2.63, 2.54, 2.2]	MC
5	25-05-2002 03:20:04–25-05-2002 04:43:52	[−0.58, −0.97, −1.08]	[2.51, 3.0, 2.47]	MC
6	25-05-2002 11:40:46–25-05-2002 12:27:28	[0.02, −0.04, −0.4]	[2.59, 2.44, 2.29]	MC
7	12-09-2004 20:33:10–13-09-2004 10:48:04	[−0.03, −0.52, −0.15]	[2.04, 2.43, 2.02]	HSS
8	17-01-2013 18:15:04–17-01-2013 20:15:04	[−0.39, −0.36, −0.11]	[2.15, 2.54, 2.0]	MC
9	17-01-2013 22:01:37–17-01-2013 23:57:37	[−0.11, −0.21, −0.39]	[2.0, 2.91, 2.47]	MC
10	28-05-2021 03:05:01–28-05-2021 07:10:20	[−0.37, −1.1, −1.02]	[2.32, 3.56, 2.67]	MC
11	24-04-2023 11:50:54–24-04-2023 13:55:15	[−1.24, −1.76, −0.72]	[2.38, 3.17, 2.08]	MC

($\alpha > 1$ and $\alpha < 1$) were often characterized using a common median value or further represented through alternative fitting approaches, such as *K*-Gaussian function. In contrast, we focused on understanding these two polytropic distributions individually, such as polytropic index greater than and less than 1. We observed that transition in median value of polytropic index from super-alfvénic to sub-alfvénic regions (see Table 1). This transition is observed in both the cases $\alpha > 1$ and $\alpha < 1$, respectively. Our observations of solar wind protons show both sub-adiabatic to super-adiabatic behaviour, which suggests periods dominated by cooling and mild-explosive to explosive behaviour , emphasizing the predominance of heating processes. This complex polytropic

Table 2. The table provides the spectral index (k_B) for the inertial and dissipation scales in super- and sub-Alfvénic regions, covering all selected events.

Sr.No.	Sub-Alfvénic Start time	Inertial scale k_B		Dissipation scale k_B	
		Super	Sub	Super	Sub
1	27-04-1999 01:52:28	−1.34	−1.54	−3.61	−3.19
2	11-05-1999 17:34:40	−2.28	1.32	−2.29	−2.55
3	20-03-2002 09:23:01	−1.63	−1.56	−2.42	−2.74
4	24-05-2002 21:01:07	−1.68	−1.48	−2.47	−2.84
5	25-05-2002 03:20:04	−1.3	−1.65	−2.3	−2.25
6	25-05-2002 11:40:46	−1.64	−1.57	−2.68	−2.29
7	12-09-2004 20:33:10	−1.83	1.49	−2.64	−2.67
8	17-01-2013 18:15:04	−1.72	−1.65	−2.13	−2.27
9	17-01-2013 22:01:37	−1.72	−1.6	−2.25	−1.92
10	28-05-2021 03:05:01	−1.65	−1.72	−2.43	−2.36
11	24-04-2023 11:50:54	−1.75	−1.85	−2.1	−1.86

behaviour suggests the presence of non-adiabatic processes. Due to the complex polytropic behaviour , multiple mechanisms are likely to contribute to the heating process. The heating mechanisms at 1 au possibly include turbulent heating, magnetic reconnection, and temperature anisotropy-driven instabilities.

3.3 Turbulence spectra

Turbulent heating is one of the prominent processes of plasma heating. In order to understand the properties of turbulence, several studies have been conducted. Previous research demonstrates that turbulence develops at 1 au, exhibiting Kolmogorov scaling $k_B^{-5/3}$ in the inertial range (R. Bruno & V. Carbone 2013). R. Bruno & L. Trenchi (2014) further observed that the Kolmogorov spectrum persists beyond 1 au, extending up to 4.5 au from the Sun. Furthermore, D. Telloni et al. (2021) found that turbulence develops between 0.1 and 1 au, whereas C. H. K. Chen et al. (2010) suggested that it is already established at 0.1 au. Both observational and simulation-based studies indicate that solar wind turbulence is weak near the Sun but gradually strengthens as the solar wind propagates outward (M. L. Goldstein, D. A. Roberts & W. H. Matthaeus 1995; R. Bruno & V. Carbone 2016; W. H. Matthaeus 2021). Several investigations have also focused on turbulence within ICMEs (R. J. Leamon, C. W. Smith & N. F. Ness 1998; L. Sorriso-Valvo et al. 2021). Specifically, K. Hamilton et al. (2008) reported a spectral index of $k_B^{-1.56}$ for ICME-magnetic clouds in the inertial range. However, there are a very limited number of studies have addressed the turbulent spectra of sub-Alfvénic regions at 1 au. For example, S. Q. Zhao et al. (2022) analysed three-dimensional magnetic power spectra of sub-Alfvénic solar wind in wavevector space using MMS observations, with a particular emphasis on characterizing turbulence anisotropy and spectral scalings at MHD scales. In contrast, our present work focuses on the turbulence spectra of both sub-Alfvénic and super-Alfvénic regions across the inertial and dissipation scales using Wind spacecraft observations. S. Q. Zhao et al. (2022) arranged the magnetic power distributions in a new coordinate system defined by the wavevector direction ($\hat{\boldsymbol{k}}$) and the background magnetic field ($\hat{\boldsymbol{b}_0}$) in Fourier space. While, we studied turbulence as a function of frequency. S. Q. Zhao et al. (2022) reported that, fluctuations perpendicular to both $\hat{\boldsymbol{k}}$ and $\hat{\boldsymbol{b}}_0$ show a strong anisotropy, with spectral index $k_{B\perp}^{-5/3}$ and $k_{B\parallel}^{-2}$ (perpendicular and parallel with respect to the magnetic field). In contrast, fluctuations lying in the $k - b_0$ plane exhibit nearly isotropic behaviour , with similar perpendicular and parallel power and spectra following $k_{B\perp}^{-3/2}$ and $k_{B\parallel}^{-3/2}$. In our analysis of sub-Alfvénic regions, we observed that, in the inertial scale the average value of spectral indices roughly follows Kolmogorov spectrum and in case of dissipation the scale average value of the spectral indices around $k_B^{-2.45}$.

In this study, we primarily focused on the investigation of magnetic field fluctuations within the inertial and dissipation scales by analysing the trace of the power spectral densities of magnetic field fluctuations across sub-Alfvénic and super-Alfvénic intervals for all eleven events. Within the inertial range (1 mHz to 0.16 Hz), the spectral indices vary from 1.3 to 2.2 for both regions, with average values ≈ 1.7 and ≈ 1.6 for the super- and sub-Alfvénic regions, respectively, see Table 2. Although both regions remain close to the Kolmogorov scale, a notable distinction emerges between the two regimes: The turbulence spectrum in the super-Alfvénic region is steeper than in the sub-Alfvénic region, indicating enhanced turbulence in super-Alfvénic flows. Interestingly, in four events (events 1, 5, 10, and 11), a contrast trend is observed where the sub-Alfvénic intervals display steeper spectral slopes compared to their super-Alfvénic counterparts within the inertial range within the same frequency range. To further explore this anomaly, for three events (1, 10, and 11) the inertial range was divided into two sub-ranges: (i) 10^{-3} to 10^{-2} Hz frequency range exhibits more turbulence in the super-Alfvénic regions as compared to sub-Alfvénic regions, while (ii) 10^{-2} to 0.16 Hz frequency range, contrasting behaviour is evident. This indicates that these 3 events exhibit more turbulence in super-Alfvénic intervals as compared to sub-Alfvénic intervals at lower frequencies, whereas less turbulence at relatively higher frequencies. However, event 5 exhibits low turbulence in the sub-Alfvénic region at different frequency range. The variation in spectral indices of magnetic field fluctuations at the inertial scale suggests that different physical processes govern turbulence in sub-Alfvénic and adjacent super-Alfvénic regions. At the dissipation scale (0.2 to 1 Hz), the spectral indices range from 1.8 to 3.6 in both regions, with mean values of ≈ 2.48 for the super-Alfvénic region and ≈ 2.45 for the sub-Alfvénic region. In most of the events, sub-Alfvénic regions have flattening spectral slopes compared to super-Alfvénic counterparts within the dissipation range. Notably, four events (*i.e.* events 2, 3, 4, and 8) display enhanced turbulence levels within the sub-Alfvénic intervals compared to the adjacent super-Alfvénic regions for the same frequency range. However, a more detailed examination reveals that Events 2 and 4 exhibit increased turbulence in the super-Alfvénic intervals compared to the sub-

Alfvénic regions, particularly within the shorter frequency range of 0.16 to 0.45 Hz. In contrast, Events 3 and 8 display steeper spectral slopes in the super-Alfvénic intervals, but over different frequency ranges. This suggests that sub-Alfvénic regions depict less turbulence compared to super-Alfvénic regions at relatively low frequencies in the dissipation scale. Note that there is a possibility of instrument noise at higher frequencies (R. P. Lepping et al. 1995; O. Alexandrova et al. 2014). The transition from a large-scale cascade to a small-scale cascade is separated by a spectral break. In our study, for most of the events, the spectral break between inertial scale and dissipation scale remains close to the proton cyclotron frequency, whereas the ion inertial length and Larmor radius remain far from the spectral break. Physical processes responsible for the generation of the spectral break are debatable. In the case where the inertial scale cascade is dominated by parallel propagating Alfvén waves, the spectral break is thought to appear at the ion cyclotron frequency (O. Alexandrova et al. 2014).

4 CONCLUSION

A thermodynamic approach to sub-Alfvénic intervals remains largely unexplored, with limited studies conducted from a polytropic perspective. Our observations suggest that the polytropic index values remain consistent during super-Alfvénic flows, i.e. in the pre- and post-sub-Alfvénic regions, whereas relative variations are observed during sub-Alfvénic flows. Interestingly, this transition in the polytropic behaviour of sub-Alfvénic regions gets influenced by their surrounding within the solar wind or ICMEs. Here, we noticed a bimodal distribution of the polytropic index, which reflects the coexistence of non-adiabatic and super-adiabatic processes, implying concurrent heating and cooling, with one process potentially prevailing over the other. Furthermore, we analysed the turbulence characteristics of the sub-Alfvénic and super-Alfvénic regions. The turbulence spectra indicate that sub-Alfvénic regions exhibit lower turbulence levels compared to adjacent super-Alfvénic regions, implying the influence of different underlying physical processes in these two regions. In this study, we focused on the thermodynamic behaviour and turbulence properties of solar wind protons, neglecting electrons or, more generally, the multiparticle description. This raises the question whether electrons and other particles exhibit similar behaviour on smaller scales or follow patterns consistent with earlier studies. Understanding the heating mechanisms in such a complicated system at a smaller scale would be challenging.

ACKNOWLEDGEMENTS

Acknowledgments: We acknowledge the instruments team members for providing the Wind MFI and 3D plasma analyser data. We appreciate the anonymous referee for constructive comments and valuable suggestions.

DATA AVAILABILITY

The data utilised in this analysis is taken from the Wind spacecraft. The Wind data are publicly available at (1) NASA's Goddard Space Flight Center (GSFC) https://wind.nasa.gov/data.php, and (2) Coordinated Data Analysis Web (CDAWeb) https://cdaweb.gsfc.nasa.gov/pub/data/wind/.

REFERENCES

Alexandrova O., Chen C. H. K., Sorriso-Valvo L., Horbury T. S., Bale S. D., 2014, in Balogh A., Bykov A., Cargill P., Dendy R., Dudok de Wit T., Raymond J., eds, Microphysics of Cosmic Plasmas. Space Sciences Series of ISSI, Vol 47, Solar Wind Turbulence and the Role of Ion Instabilities. Springer, Boston, MA, p. 25
Bale S. D., Kellogg P. J., Mozer F. S., Horbury T. S., Reme H., 2005, Phys. Rev. Lett., 94, 215002
Bandyopadhyay R. et al., 2022, ApJ, 926, L1
Borovsky J. E., Denton M. H., 2010, J. Geophys. Res. (Space Phys.), 115, A10101
Borovsky J. E., Denton M. H., Smith C. W., 2019, J. Geophys. Res. (Space Phys.), 124, 2406
Brunetti G., Lazarian A., 2007, MNRAS, 378, 245
Bruno R., Carbone V., 2013, Living Rev. Sol. Phys., 10, 2
Bruno R., Carbone V., 2016, Lecture Notes in Physics Vol. 928, Turbulence in the Solar Wind. Springer International Publishing, Switzerland
Bruno R., Trenchi L., 2014, ApJL, 787, L24
Chandran B. D. G., Verscharen D., Quataert E., Kasper J. C., Isenberg P. A., Bourouaine S., 2013, ApJ, 776, 45
Chané E., Schmieder B., Dasso S., Verbeke C., Grison B., Démoulin P., Poedts S., 2021, A&A, 647, A149
Chen C. et al., 2020, ApJS, 246, 53
Chen C. H. K., Horbury T. S., Schekochihin A. A., Wicks R. T., Alexandrova O., Mitchell J., 2010, Phys. Rev. Lett., 104, 255002
Chen C. H. K., Leung L., Boldyrev S., Maruca B. A., Bale S. D., 2014, Geophys. Res. Lett., 41, 8081
Crooker N. U., Shodhan S., Gosling J. T., Simmerer J., Lepping R. P., Steinberg J. T., Kahler S. W., 2000, Geophys. Res. Lett., 27, 3769
D'Amicis R. et al., 2025, A&A, 693, A243
Dayeh M. A., Livadiotis G., 2022, ApJ, 941, L26
Dimmock A. P., Osmane A., Pulkkinen T. I., Nykyri K., Kilpua E., 2017, J. Geophys. Res. (Space Phys.), 122, 6165
Durney B., 1972, Ap&SS, 17, 489
Echim M. et al., 2021, in Maggiolo R., André N., Hasegawa H., Welling D. T., eds, Magnetospheres in the Solar System. Wiley, New York, p. 67
Elliott H. A. et al., 2019, ApJ, 885, 156
Elmegreen B. G., Scalo J., 2004, ARA&A, 42, 211
Ervin T. et al., 2024, ApJ, 972, 129
Ghag K. et al., 2025, Adv. Space Res., 75, 1371
Goldstein M. L., Roberts D. A., Matthaeus W. H., 1995, ARA&A, 33, 283
Gosling J. T., Asbridge J. R., Bame S. J., Feldman W. C., Zwickl R. D., Paschmann G., Sckopke N., Russell C. T., 1982, J. Geophys. Res., 87, 239
Hajra R., Tsurutani B. T., 2022, ApJ, 926, 135
Hamilton K., Smith C. W., Vasquez B. J., Leamon R. J., 2008, J. Geophys. Res. (Space Phys.), 113, A0110
Hasegawa H., Denton R. E., Chen L. J., Hu Q., Nishino M. N., Hwang K. J., 2024, J. Geophys. Res. (Space Phys.), 129, 2024JA033395
Hutchinson J. A., Wright D. M., Milan S. E., 2011, J. Geophys. Res. (Space Phys.), 116, A09211
Iroshnikov P. S., 1964, Sov. Astron., 7, 566
Jagarlamudi V. K., Braga C. R., Raouafi N. E., Vourlidas A., 2025, ApJ, 989, 133
Janardhan P., Fujiki K., Sawant H. S., Kojima M., Hakamada K., Krishnan R., 2008, J. Geophys. Res. (Space Phys.), 113, A03102
Jiao Y., Liu Y. D., Cheng W., Ran H., Wang R., 2024, ApJ, 975, L41
Kartalev M., Dryer M., Grigorov K., Stoimenova E., 2006, J. Geophys. Res. (Space Phys.), 111, A10107
Kasper J. C. et al., 2021, Phys. Rev. Lett., 127, 255101
Katsavrias C., Nicolaou G., Di Matteo S., Kepko L., Viall N. M., Aminalragia-Giamini S., Livadiotis G., 2024, A&A, 686, L10
Katsavrias C., Nicolaou G., Livadiotis G., Vourlidas A., Wilson L. B. III, Sandberg I., 2025a, A&A, 695, A146
Katsavrias C., Nicolaou G., Verscharen D., Livadiotis G., 2025b, A&A, 701, A151

Khuntia S., Mishra W., Mishra S. K., Wang Y., Zhang J., Lyu S., 2023, ApJ, 958, 92
Khuntia S., Mishra W., Wang Y., Mishra S. K., Nieves-Chinchilla T., Lyu S., 2024, MNRAS, 535, 2585
Khuntia S., Mishra W., Agarwal A., 2025, A&A, 698, A79
Kolmogorov A., 1941a, Akademiia Nauk SSSR Doklady, 30, 301
Kolmogorov A., 1941b, CR Acad. Sci. URSS, 30, 301
Kraichnan R. H., 1965, Physics of Fluids, 8, 1385
Leamon R. J., Smith C. W., Ness N. F., 1998, Geophys. Res. Lett., 25, 2505
Lepping R. P. et al., 1995, Space Sci. Rev., 71, 207
Lin R. P. et al., 1995, Space Sci. Rev., 71, 125
Livadiotis G., 2016, ApJS, 223, 13
Livadiotis G., 2018, J. Geophys. Res. (Space Phys.), 123, 1050
Livadiotis G., 2019, Entropy, 21, 1041
Livadiotis G., Desai M. I., 2016, ApJ, 829, 88
Livadiotis G., McComas D. J., 2023, ApJ, 956, 88
Livadiotis G., Nicolaou G., 2021, ApJ, 909, 127
Lugaz N., Farrugia C. J., Huang C.-L., Winslow R. M., Spence H. E., Schwadron N. A., 2016, Nat. Commun., 7, 13001
Manu V., Balan N., Zhang Q.-H., Xing Z.-Y., 2023, Space Weather, 21, e2022SW003314
Masías-Meza J. J., Dasso S., Démoulin P., Rodriguez L., Janvier M., 2016, A&A, 592, A118
Matthaeus W. H., 2021, Phys. Plasmas, 28, 032306
Matthaeus W. H., Zank G. P., Smith C. W., Oughton S., 1999, Phys. Rev. Lett., 82, 3444
Matthaeus W. H., Breech B., Dmitruk P., Bemporad A., Poletto G., Velli M., Romoli M., 2007, ApJ, 657, L121
Mishra W., Wang Y., Teriaca L., Zhang J., Chi Y., 2020, Front. Astron. Space Sci., 7, 1
Nicolaou G., Livadiotis G., 2019, ApJ, 884, 52
Nicolaou G., Livadiotis G., Moussas X., 2014, Sol. Phys., 289, 1371
Nicolaou G., Livadiotis G., Wicks R. T., 2019, Entropy, 21, 997
Nicolaou G., Livadiotis G., Wicks R. T., Verscharen D., Maruca B. A., 2020, ApJ, 901, 26
Nicolaou G., Livadiotis G., Desai M. I., 2021, Appl. Sci., 11, 4019
Ofman L. et al., 2023, ApJ, 954, 109
Osherovich V. A., Farrugia C. J., Burlaga L. F., Lepping R. P., Fainberg J., Stone R. G., 1993, J. Geophys. Res., 98, 15331
Park J.-S., Shue J.-H., Nariyuki Y., Kartalev M., 2019, J. Geophys. Res. (Space Phys.), 124, 1866
Paulson K. W. et al., 2023, AGU Fall Meeting Abstracts. p. SH31D–2999
Regnault F., Janvier M., Démoulin P., Auchère F., Strugarek A., Dasso S., Noûs C., 2020, J. Geophys. Res. (Space Phys.), 125, e28150
Richard L., Sorriso-Valvo L., Yordanova E., Graham D. B., Khotyaintsev Y. V., 2024, Phys. Rev. Lett., 132, 105201
Sahraoui F., Belmont G., Rezeau L., Cornilleau-Wehrlin N., Pinçon J. L., Balogh A., 2006, Phys. Rev. Lett., 96, 075002
Shaikh Z. I., 2024, MNRAS, 530, 3005
Shaikh Z. I., Raghav A. N., Vichare G., D'Amicis R., Telloni D., 2023a, MNRAS, 519, L62
Shaikh Z. I., Vichare G., Bhaskar A., Raghav A. N., Bourouaine S., 2023b, ApJ, 959, 50
Smith C. W., Mullan D. J., Ness N. F., Skoug R. M., Steinberg J., 2001, J. Geophys. Res., 106, 18625
Sorriso-Valvo L. et al., 2007, Phys. Rev. Lett., 99, 115001
Sorriso-Valvo L., Yordanova E., Dimmock A. P., Telloni D., 2021, ApJ, 919, L30
Telloni D. et al., 2021, ApJ, 912, L21
Totten T. L., Freeman J. W., Arya S., 1995, J. Geophys. Res., 100, 13
Usmanov A. V., Goldstein M. L., Ogilvie K. W., Farrell W. M., Lawrence G. R., 2005, J. Geophys. Res. (Space Phys.), 110, A01106
Verdini A., Velli M., 2007, ApJ, 662, 669
Verdini A., Velli M., Buchlin E., 2009, ApJ, 700, L39
Yang Y., Wan M., Matthaeus W. H., Sorriso-Valvo L., Parashar T. N., Lu Q., Shi Y., Chen S., 2019, MNRAS, 482, 4933
Yermolaev Y. I., Nikolaeva N. S., Lodkina I. G., Yermolaev M. Y., 2010, Ann. Geophys., 28, 2177
Yermolaev Y. I., Lodkina I. G., Nikolaeva N. S., Yermolaev M. Y., 2015, J. Geophys. Res. (Space Phys.), 120, 7094
Yokoyama N., Kamide Y., 1997, J. Geophys. Res., 102, 14215
Yordanova E., Vörös Z., Sorriso-Valvo L., Dimmock A. P., Kilpua E., 2021, ApJ, 921, 65
Zank G. P., Dosch A., Hunana P., Florinski V., Matthaeus W. H., Webb G. M., 2012, ApJ, 745, 35
Zank G. P., Zhao L.-L., Adhikari L., Telloni D., Kasper J. C., Stevens M., Rahmati A., Bale S. D., 2022, ApJ, 926, L16
Zank G. P. et al., 2024, ApJ, 966, 75
Zhang G.-L., 1996, Chinese Astron. Astrophys., 20, 482
Zhang J. et al., 2022, ApJ, 937, 70
Zhao L.-L., Zank G. P., Telloni D., Stevens M., Kasper J. C., Bale S. D., 2022a, ApJ, 928, L15
Zhao L.-L., Zank G. P., Adhikari L., Telloni D., Stevens M., Kasper J. C., Bale S. D., Raouafi N. E., 2022b, ApJ, 934, L36
Zhao S. Q., Yan H., Liu T. Z., Liu M., Wang H., 2022, ApJ, 937, 102
Zhu X., Zank G. P., Zhao L., Silwal A., 2025, ApJ, 978, L34

APPENDIX A: SUB-ALFVENIC REGIONS EMBEDDED WITHIN INTERPLANETARY STRUCTURES

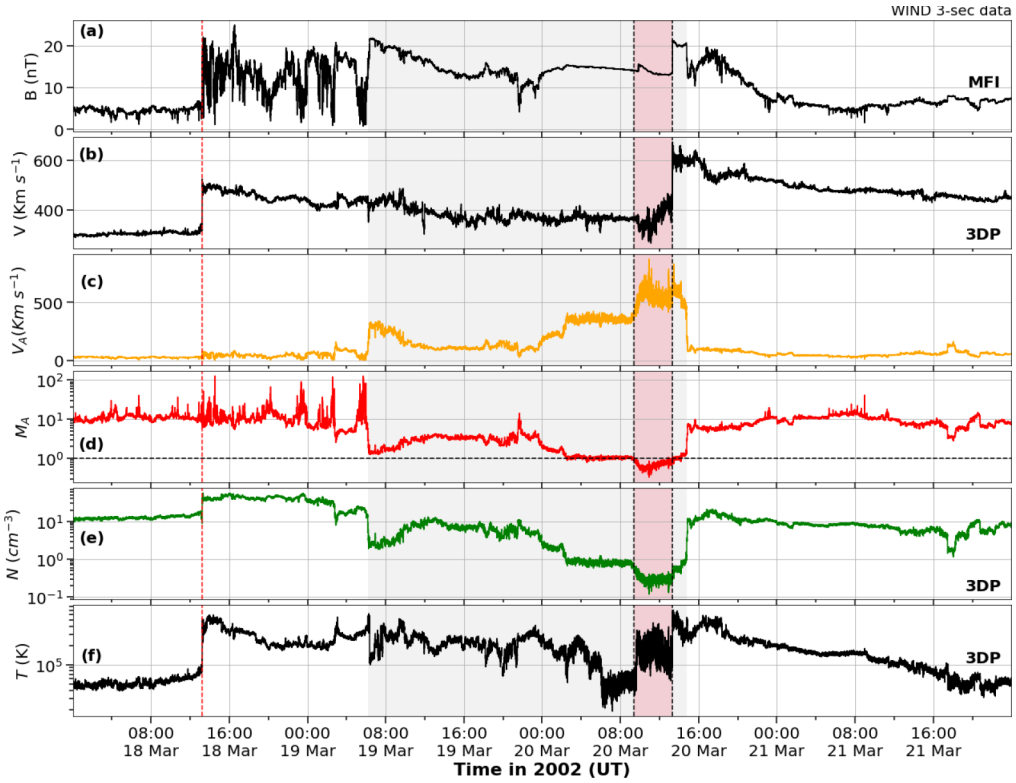

Figure A1. This figure represents the sub-Alfvénic region embedded within ICME–MC and the event occurred on 2002 March 20. The red vertical line shows the onset of the ICME. The grey shaded region shows the MC, and the pink shading exhibits the sub-Alfvénic interval within the MC.

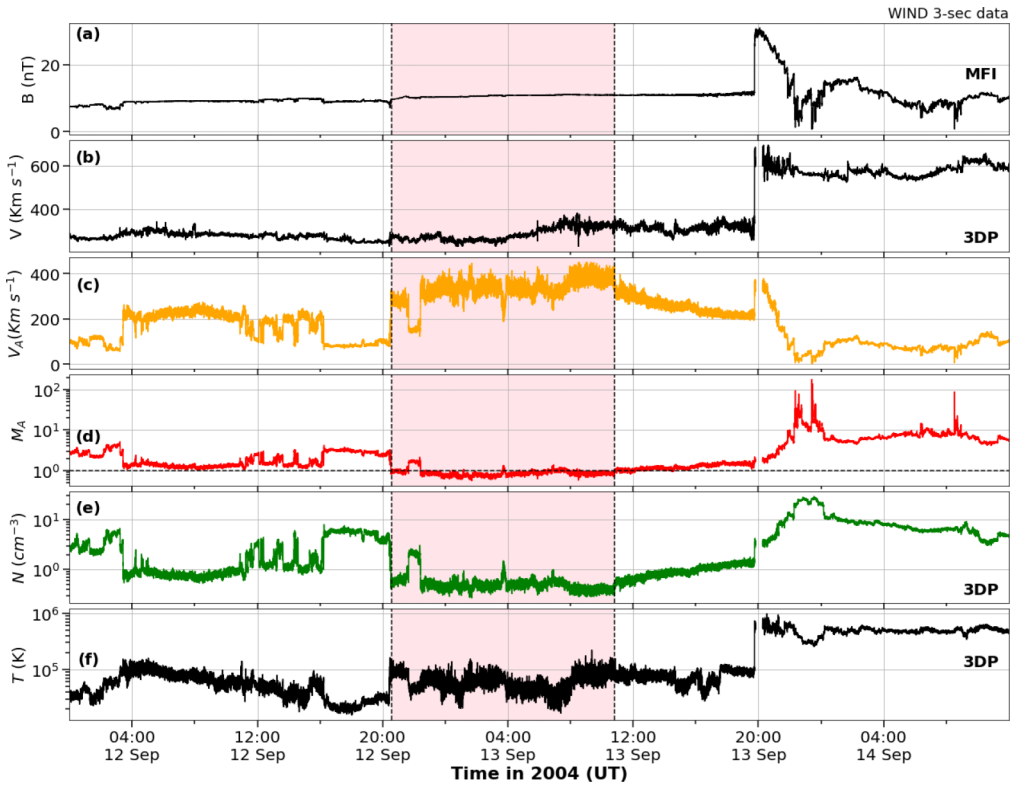

Figure A2. This figure represents sub-Alfvénic region embedded within HSS and event occurred on 2004 September 12. Here, pink shading exhibits sub-Alfvenic interval.

APPENDIX B: POLYTOPIC NATURE

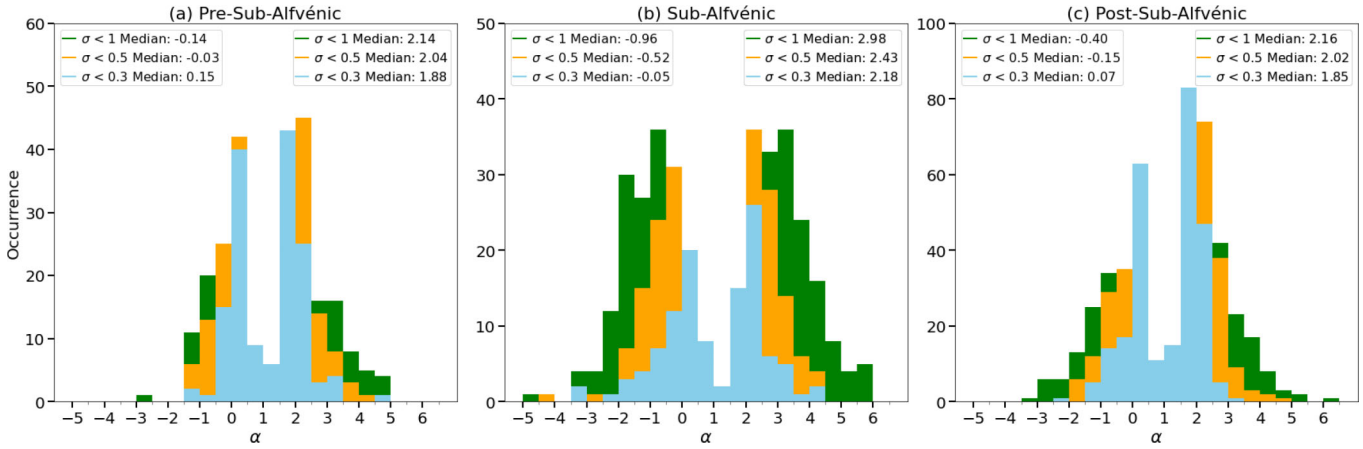

Figure B1. This figure represents histogram plot of event occurred on 12 September 2004. This figure is similar to Fig. 4.

This paper has been typeset from a TEX/LATEX file prepared by the author.